Materials Horizons

ROYAL SOCIETY OF CHEMISTRY

COMMUNICATION

View Article Online
View Journal

Cite this: DOI: 10.1039/d6mh00161k

Received 28th January 2026,
Accepted 17th March 2026

DOI: 10.1039/d6mh00161k

rsc.li/materials-horizons

In-operando dipole orientation for bipolar injection from air-stable electrodes into organic semiconductors

Anton Kirch, *[a] Joan Ràfols-Ribé, [a] Yuntao Qiu,[a] Thushar Salkod Mahabaleshwar,[ac] William Strömberg,[a] Ajay Kumar Poonia,[abc] Preetam Dacha,[a] Kumar Saumya,[a] Sri Harish Kumar Paleti, [ac] Christian Larsen, [a] Nicolò Maccaferri [bc] and Ludvig Edman [ac]

Efficient charge-carrier injection from air-stable electrodes into organic semiconductors (OSCs) is essential for fabricating solution-processed organic electronic devices under ambient conditions. Today, this is typically achieved by incorporating doped OSC interlayers, introducing self-assembled dipole monolayers, or adding mobile ions to the active material (AM). Here, we demonstrate an alternative approach that eliminates the need for additional injection layers or ionic additives. We achieve this by blending the dipolar compound TMPE-OH into the electroluminescent polymer Super Yellow (SY) and depositing this sole AM between two air-stable electrodes, forming a single-layer, dipole-doped OLED (D-OLED). By tracking its transient voltage-luminance response, performing impedance spectroscopy, and comparing these characteristics with two other single-layer device concepts, *i.e.* a neat-SY OLED without a dipolar compound and a light-emitting electrochemical cell (LEC) containing mobile ions, we can establish that the auxiliary dipoles in the D-OLED reorient under the applied driving voltage, enabling fast luminance turn-on and thinning the injection barriers at both electrodes. Finally, we demonstrate that the D-OLED achieves current efficacies comparable to those of SY OLEDs incorporating dedicated injection layers or LECs. Our study establishes dipolar doping as a practical strategy for efficient bipolar charge injection from air-stable electrodes in solution-processed organic semiconductor devices.

New concepts

Realizing charge-carrier transfer between air-stable electrode materials (such as Al or ITO) and organic semiconductors is crucial for processing organic devices from solution under ambient conditions. This typically requires additional interlayers, such as doped films or dipolar self-assembled monolayers, for efficient charge transfer. However, the resulting multi-layer stacks are difficult to implement because solution processing is inherently limited in precision. A concept that combines air stability with minimal stack complexity is consequently a fundamental objective. We propose such a concept by doping a dipolar compound into the bulk of the organic semiconductor (OSC). For the showcase of a single-layer OLED (ITO/organic film/Al), we prove that the dipolar compound reorients reversibly under the applied operating voltage and realizes bipolar charge-carrier injection without any additional injection layer. Our concept uses merely the device's operating voltage (<10 V) and is applicable to any ink deposition technique. Our findings establish an innovative concept for charge-carrier transfer between electrode materials and OSCs. This reshapes the view on the requirements for organic optoelectronic device production and offers a practically relevant route for their low-cost fabrication. The conceptual nature of our manuscript makes it a good fit for Materials Horizons.

Introduction

Organic semiconductors with tailored properties have enabled the rapid development of organic devices like light-emitting diodes (OLEDs),[1,2] photovoltaics (OPVs),[3,4] transistors,[5,6] photodetectors (OPDs),[7] or sensors.[8,9] These concepts are attractive because they combine high performance with mechanical flexibility,[10] biocompatibility,[11] and offer pathways towards low-cost fabrication from solution under ambient conditions.[12,13] Considering device processability and stability, it is therefore desirable to use air-stable materials for achieving charge-carrier injection into the OSC. This is typically realized by introducing dedicated interface layers, such as electronically doped OSCs[14,15] and dipolar self-assembled monolayers (SAMs),[16,17] or mobile ions into the bulk of the AM.[18] The inclusion of an extra layer, however, exacerbates material recycling and complicates device fabrication under ambient conditions, or even prohibits it when the included material is air-sensitive. Dipolar SAMs further pose the risk that the dipoles reorient in a direction that inhibits charge transfer.[19,20] The mobile-ion approach is limited by its dependence on salt dissolution and ion migration through the bulk to form injection-facilitating electric double layers (EDLs).[21]

[a] *The Organic Photonics and Electronics Group, Department of Physics, Umeå University, SE-90187 Umeå, Sweden. E-mail: anton.kirch@umu.se*
[b] *Ultrafast Nanoscience Group, Department of Physics, Umeå University, SE-90187 Umeå, Sweden*
[c] *Wallenberg Initiative Materials Science for Sustainability, Department of Physics, Umeå University, SE-90187 Umeå, Sweden*

Such long-range transfer of bulky ions can cause detrimental morphological changes and electrochemical (EC) side reactions.[22]

In this context, recent attempts to polarize the AM by an electric field (*E*-field) during fabrication are interesting. In 2024, Cui and co-workers reported that the morphology of the AM in OPVs can be tuned by applying a high external *E*-field in the wet solution state during ambient-air coating, resulting in an improved power conversion efficiency.[23] Zhao *et al.* reported on a similar wet orientation of ion-transporting monomers in an applied *E*-field, followed by photochemical curing to freeze the dipole orientation, for the construction of solid-state batteries with vertically aligned ion-transport pathways.[24] Also in 2024, Rodriguez-Lopez and colleagues used molecular dynamics simulations to establish the conditions under which dipolar OSC molecules orient in the direction of an *E*-field applied during vapor deposition.[25] Finding the optimal molecular orientation state, however, is nontrivial. For instance, light extraction from OLEDs and absorption in OPVs benefit from a horizontal (parallel to the electrode surface) orientation of the transition dipole moment, while efficient charge injection and extraction require vertically oriented permanent dipole moments.[26]

Here, we present an alternative generic approach for efficient charge transfer between two air-stable electrodes and a solid single-layer AM. It builds on the idea by Hofmann *et al.* to dope polar molecules into a non-polar host to facilitate charge injection, referred to as dipolar doping.[20] They investigated dense films fabricated by thermal evaporation and found a built-in (static after fabrication) impact of the resulting giant surface potential on the hole injection. By contrast, we use a solution-processed polymer host complemented with an auxiliary, electronically insulating dipolar compound. This configuration yields polar reorientation of the dipolar compound by the low applied driving voltage and thus dynamic (the effect is only present under device operation) bipolar injection while keeping the OSCs orientation unaltered. The presented concept is compatible with solution-based fabrication under ambient conditions, does not incorporate mobile ions that can compromise the device performance, does not require high voltages under fabrication, and avoids additional interlayers that increase the stack complexity.

Results

Conception

In this work, we aim to understand the functionality of dipolar doping by fabricating a dipole-doped single-layer OLED (D-OLED) and comparing its performance with two other single-layer device concepts, *i.e.* a neat-SY OLED (N-OLED) and an LEC. The N-OLED comprises neither injection- nor transport-facilitating additives, thus representing the most primitive single-layer device. The LEC contains mobile ions that enable both low injection and transport resistance, owing to EDL formation and EC doping, without the need for additional layers.

Fig. 1(a) displays the device structure used for all devices throughout this work. It comprises a glass substrate, a transparent indium tin oxide (ITO) anode (145 nm thick), a single AM film (thickness $d_{AM} \approx 120$ nm), and a reflective Al top cathode (100 nm). The pixel dimensions are 2×2 mm^2. Fig. 1(b) presents the work functions of the electrode materials[27] and the highest occupied molecular orbital (HOMO) and lowest unoccupied molecular orbital (LUMO) levels of the employed organic materials, as determined by cyclic voltammetry, *cf.* SI Section S1. Fig. 1(c) sketches how the dipolar molecules in the D-OLED reorient under the impact of the applied operating voltage and facilitate charge-carrier injection. The chemical structures of the AM constituents are shown in Fig. 1(d): the electroluminescent copolymer Super Yellow (SY) as OSC, the dipolar hydroxyl-capped trimethylolpropane ethoxylate (TMPE-OH), and the salt KCF_3SO_3.

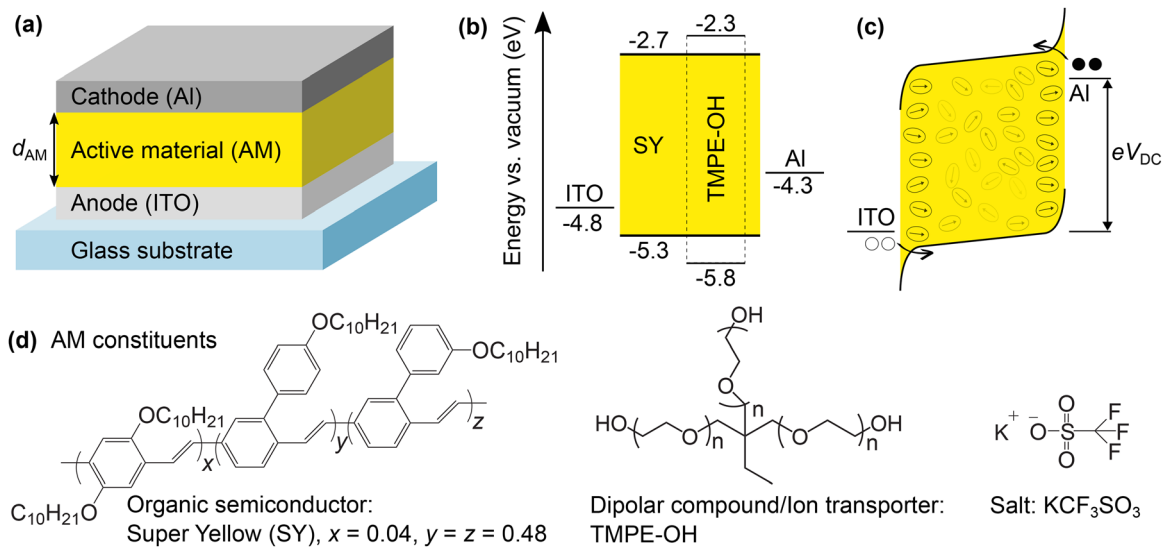

Fig. 1 (a) Sketch of the device structure used in this work. (b) Work functions of the electrode materials[27] and HOMO/LUMO levels of SY and TMPE-OH, *cf.* SI Section S1. (c) Dipole-mitigated injection mechanism of the D-OLED under applied bias V_{DC}. (d) Chemical structures of the AM constituents.

Table 1 AM constituents and mass ratios used for the five devices employed in this work

Device	Abbreviation	Mass ratio		
		Super yellow	TMPE-OH	KCF_3SO_3
Neat-SY OLED	N-OLED	1	—	—
Dipole OLED	D-OLED	1	0.4	—
LEC Low salt	L-LEC	1	0.4	0.005
Medium salt	M-LEC	1	0.4	0.03
High salt	H-LEC	1	0.4	0.05

The three single-layer electroluminescent device concepts are realized by varying the AM constituents. We fabricate

(i) a neat-SY OLED (N-OLED), where the AM contains only SY,

(ii) a dipole OLED (D-OLED), the subject of this study, comprising SY and TMPE-OH,

(iii) three LECs, where the AM consists of SY, TMPE-OH, and salt at three differing salt loads, referred to as low (L), medium (M), and high (H) salt LEC.

Please refer to Table 1 for the specific mass ratios and device abbreviations. We use a TMPE-OH concentration of 40 wt% compared to SY, which is higher than what we usually use for LECs,[28,29] to stay consistent with the optimum TMPE-OH concentration found for the D-OLED.

Voltage-luminance transients

Fig. 2 presents the transients of (a) the driving voltage and (b) the forward luminance for the five pristine devices operated at a constant current of 0.31 mA (corresponding to a current density of 7.7 mA cm^{-2}). The N-OLED exhibits a high driving voltage of about 20 V and a faint, constant luminance below 10 cd m^{-2}. This is the expected behavior of a simple polymer OLED, with its high driving voltage caused by the large injection barriers, *cf.* Fig. 1(b), and the low electron and hole conductivity of undoped SY.[30] We attribute the poor luminance to an unbalanced charge-carrier distribution, owing to the mismatched injection barriers, *i.e.* 1.6 eV for electrons *vs.* 0.5 eV for holes.

The three LECs (open symbols in Fig. 2) reach a driving voltage slightly below 3 V within a few seconds, which is close to the EC energy gap of SY (E_{SY} = 2.6 eV), *cf.* Fig. 1(b). This indicates low injection and transport resistance. In other words, the LECs quickly form EDLs and EC-doped layers, operating close to their theoretical voltage minimum. As expected, their luminance rises during the initial operation. Increasing the salt concentration decreases the turn-on time to peak luminance but also accelerates the onset of the luminance drop. The latter can be assigned to doping-induced exciton quenching and/or electrolyte-induced device degradation. These findings are in agreement with the established LEC understanding.[28,31]

The behavior of the D-OLED is surprising, considering that it features the same injection barriers as the other four devices. Although it is free of mobile ions, it exhibits voltage and luminance transients that indicate changes in the AM's electrical properties. The driving voltage initially decreases and reaches a minimum of 3.8 V after 340 s, a 16 V reduction relative to the N-OLED. Moreover, it turns on quickly, reaching 280 cd m^{-2} after 170 s. This value is comparable to the LECs' luminance and 50 times brighter than the N-OLED.

Fig. S2 presents a zoom into the first seconds of operation for pristine pixels of the same devices as in Fig. 2, driven at 1 mA (25 mA cm^{-2}). Here, we use different experimental equipment that allows us to track the turn-on characteristics at higher time resolution. We observe that, although the D-OLED initially requires a high driving voltage of approximately 14 V, it reduces to moderate voltages below 6 V within 2 s.

Given the transient behavior of the D-OLED during initial operation, it is possible to consider ionic impurities in the TMPE-OH as a potential cause. However, the supplier of TMPE-OH reports that the upper limit of potential ionic impurities is below 100 ppm,[32] which corresponds to a ~16 times lower ion concentration than in the L-LEC. Following the salt-concentration trend observed in Fig. 2(b), such an ion concentration would yield a dramatically slower device turn-on of the D-OLED compared to the LECs, which is not the case. It thus seems unlikely that ionic impurities are responsible for the D-OLED behavior.

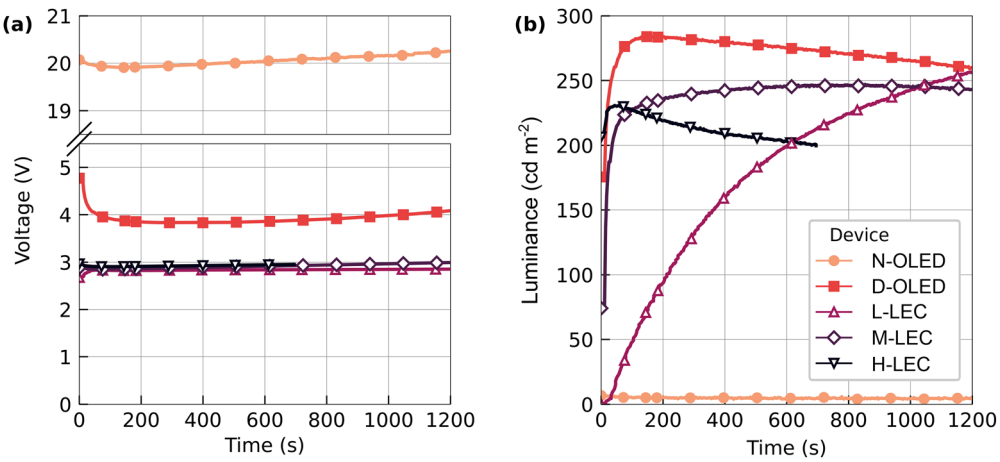

Fig. 2 Temporal evolution of (a) the driving voltage and (b) the forward luminance for the five devices driven at a constant current of 0.31 mA (7.7 mA cm^{-2}) using a voltage compliance of 21 V.

We deduce that charge-carrier injection and/or transport in the D-OLED work more effectively than in the N-OLED after only a few seconds, although it does not reach the electrical performance of the LECs. Further, its charge-carrier distribution seems to be more balanced compared to the N-OLED, allowing electron injection and exciton recombination away from the electrode interfaces, resulting in significant forward luminance and rapid turn-on. Both the voltage and luminance transients indicate that the D-OLED's AM properties are not static, like in a classical p–i–n OLED.[33] This is surprising, as no mobile ions are present in the system, and raises the question of how the dipolar compound acts under an applied E-field. To better understand this, we investigate the dynamic processes in all devices *via* impedance spectroscopy (IS).[34]

Impedance spectroscopy at short-circuit conditions

Here, we perturb pristine devices with a small AC voltage (V_{AC}, RMS = 20 mV), using a DC bias V_{DC} = 0 V, after letting them stabilize at a temperature T = 25 ± 0.2 °C for 60 s. The AC frequency f is swept from 100 kHz to 10 mHz and back to 100 kHz, with a full sweep taking about 40 min.

Fig. 3(a and b) present back-and-forth scans of the IS data (absolute impedance $|Z|$ and current-to-voltage phase shift φ). For all devices, no significant forward-backward hysteresis is visible, indicating that they are measured at steady conditions. Fig. 3(c) shows the same data, but represented as the effective capacitance density

$$C = \frac{1}{A\omega}\mathrm{Im}\left(\frac{1}{Z}\right) = \frac{-X}{A\omega|Z|^2} \quad (1)$$

with the reactance X = Im(Z), the pixel area A = 4 mm^2, and the angular frequency $\omega = 2\pi f$, *cf.* SI Section S3.

The N-OLED acts like a capacitor over the investigated frequency range. That is, $|Z|$ scales inversely with f, and φ is constant at −90°. Using the formula for the parallel-plate capacitance density

$$C = \frac{\varepsilon_0\varepsilon_r}{d} \quad (2)$$

and the experimentally determined values C = 23 nF cm^{-2} at 100 kHz (Fig. 3c) and $d = d_{AM}$ = 120 ± 5 nm (Table 2), we can extract ε_r = 3.1 ± 0.1 for SY. This value is in agreement with previous reports.[35,36] The capacitance given by the geometric dimension d_{AM} and the relative permittivity ε_r at high frequencies is commonly referred to as geometric capacitance density C_{geo}. Here, we use the values found at the upper limit of the investigated IS frequency window, $C_{geo} = C(f = 100\ \mathrm{kHz})$.

The D-OLED shows two distinctions from the N-OLED: First, C_{geo} increases slightly (Fig. 3c), implying a larger ε_r, which can be attributed to the polar TMPE-OH. Second, the phase angle increases at lower frequencies, reaching $\varphi \approx -40°$ at 10 mHz (Fig. 3b). This finding is indeed interesting, as it points to a

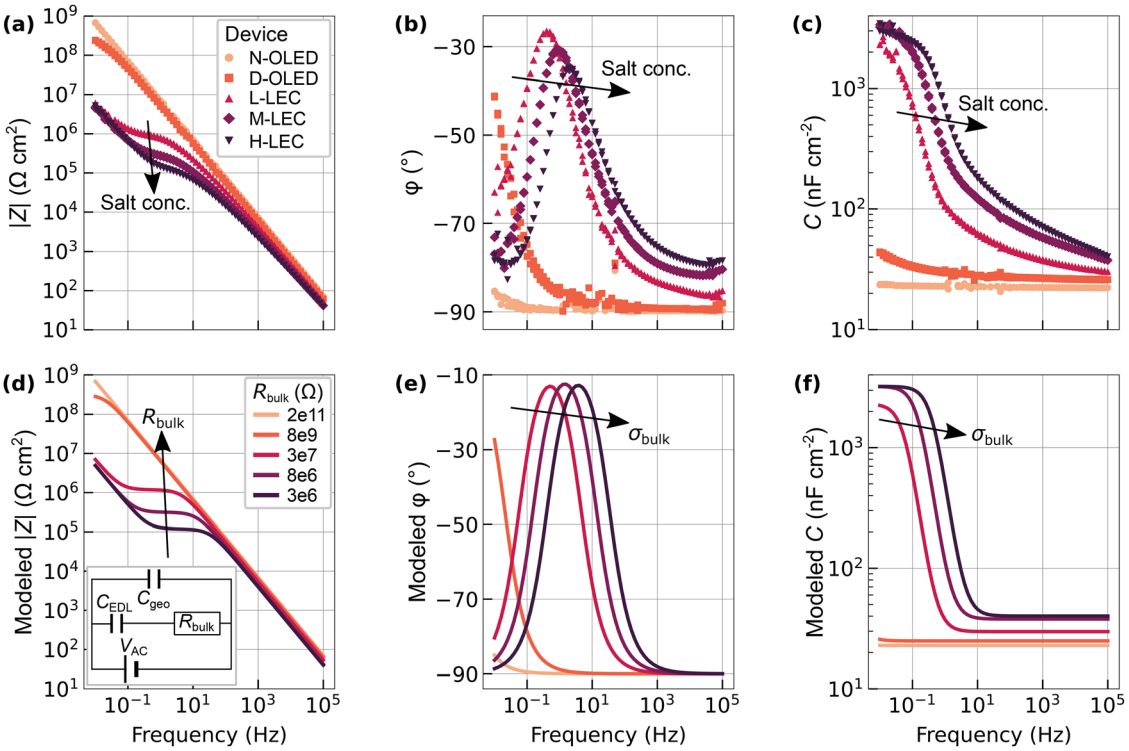

Fig. 3 Impedance characteristics obtained from (a–c) the measurement and (d–f) the equivalent circuit model (ECM) shown in the inset in (d). The data are taken at V_{DC} = 0, with a V_{AC} RMS = 20 mV at T = 25 °C. The legend in (a) specifies the tested devices, and the legend in (d) shows the R_{bulk} used as the free parameter in the ECM.

Table 2 Device parameters for the five investigated devices. d_{AM} is measured with a profilometer, C_{geo} and C_{EDL} are the values measured at the indicated frequencies *via* IS. From d_{AM} and C_{geo}, we derive ε_r *via* eqn (2). From the ECM, *cf.* Fig. 3(d), we determine R_{bulk} (here displayed as σ_{bulk}), used as the only fitting parameter. The indicated uncertainties originate from the d_{AM} variations of ± 5 nm

	Measured			Derived	
Device	d_{AM} (nm)	C_{geo} (nF cm^{-2}) at 100 kHz	C_{EDL} (nF cm^{-2}) at 10 mHz	ε_r at 100 kHz	σ_{bulk} (S m^{-1})
N-OLED	120 ± 5	23	—	3.1 ± 0.1	$<1.5 \times 10^{-13}$
D-OLED	128 ± 5	25	—	3.6 ± 0.2	4×10^{-12}
L-LEC	128 ± 5	30	2300	4.3 ± 0.2	1.1×10^{-9}
M-LEC	124 ± 5	37	3200	5.3 ± 0.2	3.9×10^{-9}
H-LEC	106 ± 5	40	3200	4.8 ± 0.2	8.8×10^{-9}

slow relaxation process in the AM. It can be rationalized by TMPE-OH being a polar molecule, featuring three polar OH end groups and an ester backbone that can reorient in an *E*-field. Such segmental chain reorientation under AC perturbation has been studied in similar molecules like poly(ethylene glycol) (PEG) or poly(ethylene oxide) (PEO).[37,38]

Regarding the LECs, introducing mobile ions into the AM clearly alters the IS characteristics and illustrates that their device physics is fundamentally different from the D-OLED. At high frequencies, C_{geo} increases relative to the N-OLED, as ions enhance the AM's dielectric response. At $f_c \approx 1$ Hz, all LECs exhibit a characteristic φ peak and a $|Z|$ plateau, *cf.* Fig. 3(a and b). At this point, the ionic conductivity

$$\sigma_{bulk} = \frac{d_{AM}}{A \cdot R_{bulk}} \propto f_c \quad (3)$$

governs the device impedance.[39] At frequencies $f < f_c$, the three impedance curves collapse back into a single line. Here, the ions have enough time to accumulate at the electrode interfaces, and the EDL capacitance becomes dominant.[40]

To gain a better understanding of the measured data, we use a Debye equivalent circuit model (ECM), *cf.* inset in Fig. 3(d), to reproduce all five device characteristics. This is a common approach to determine the ionic conductivity in polymer electrolytes for the case of blocking electrodes.[41] It comprises merely three elements in its simplest form: the geometric capacitance C_{geo}, the EDL capacitance C_{EDL}, and the resistance (or conductivity) of the AM bulk, here termed R_{bulk} (σ_{bulk}), *cf.* eqn (3). We neglect an additional series resistance, because the impedance of our samples exceeds the resistive contributions of the wiring and electrodes. Modeling the EDL as a capacitor and omitting the use of a Randles circuit is reasonable at V_{DC} = 0, as electronic charge carriers cannot be injected into the OSC (non-faradaic system), considering their significant injection barriers, *cf.* Fig. 1(b).[34] We choose to model all five devices with the same ECM to achieve a more intuitive basis for comparison. For the N-OLED and D-OLED, the implementation of C_{EDL} is unreasonable, as they do not comprise mobile ions and hence reach no EDL capacitance plateau at low frequencies (*cf.* Fig. 3(c), indicated by "—" in Table 2). This is reflected in the ECM by setting their C_{EDL} to infinity (high values in the implementation). The full set of ECM parameters can be found in the SI Section S4.

As presented in Fig. 3(d–f), the IS measurements can be captured qualitatively, and mostly even quantitatively, by this simplistic ECM for all five devices. C_{geo} dominates the impedance at high frequencies and is set equal to the measured C_{geo} (*cf.* Table 2). When approaching the characteristic frequency f_c for the LECs, the ion or bulk resistance R_{bulk} limits the current.[39] For better comparison, Table 2 displays the respective geometry-independent conductivity values σ_{bulk}, connected to R_{bulk} *via* Eqn (3). In the ECM, R_{bulk} is the only free parameter and is chosen such that the modeled IS characteristics resemble the measured data. At low frequencies ($f < f_c$), C_{EDL} limits the current for the LECs and is set equal to the measured value, *cf.* Table 2. For the N-OLED and D-OLED, C_{EDL} is set to infinity (a random high value).

While all LECs show a clear C_{EDL} plateau, no EDL formation is detected for the N-OLED and D-OLED. This is consistent with the absence of mobile ions in these systems. Furthermore, σ_{bulk} of the D-OLED, which we can extract from the ECM as the only free parameter, is about 3 orders of magnitude smaller than for the LECs. This supports that the impurity ion concentration is insignificant in the D-OLED. It exhibits, however, a slow relaxation process at low frequencies. This stands in contrast to the N-OLED, which displays a capacitor-like behavior, and indicates that TMPE-OH dipoles slowly reorient in the AM, giving rise to a motion of electric charge.

Impedance spectroscopy under bias

In the previous section, we probed the devices using impedance spectroscopy at V_{DC} = 0 and observed a dipolar relaxation process in the D-OLED. Now, we compare the impedance response of an LEC (the M-LEC as an example) with the D-OLED under increasing bias to learn more about their characteristics under operating conditions. We first let the device stabilize for 20 min at a given V_{DC} and then perform an IS scan with V_{AC} superimposed on V_{DC}. The impedance is measured on pristine devices, with the *f* running from 100 kHz to 100 mHz and back to 100 kHz. Again, we observe no significant forward-backward hysteresis. For $V_{DC} \gg 0$ V, electronic charge carriers are injected into the system, and we can no longer treat it as non-faradaic. Hence, the ECM presented in Fig. 3(d) does not hold for this investigation.

Fig. 4 compares the IS data of (a–c) the M-LEC with (d–f) the D-OLED. Please find the data for the N-OLED, L-LEC, and H-LEC in the SI, Fig. S6. For the LEC, the impedance characteristics (C_{geo}, C_{EDL}, and f_c) remain constant for $V_{DC} < E_{SY}/e$ = 2.6 V (e is the elementary charge). Here, charge carrier injection is insignificant, and the general device structure stays

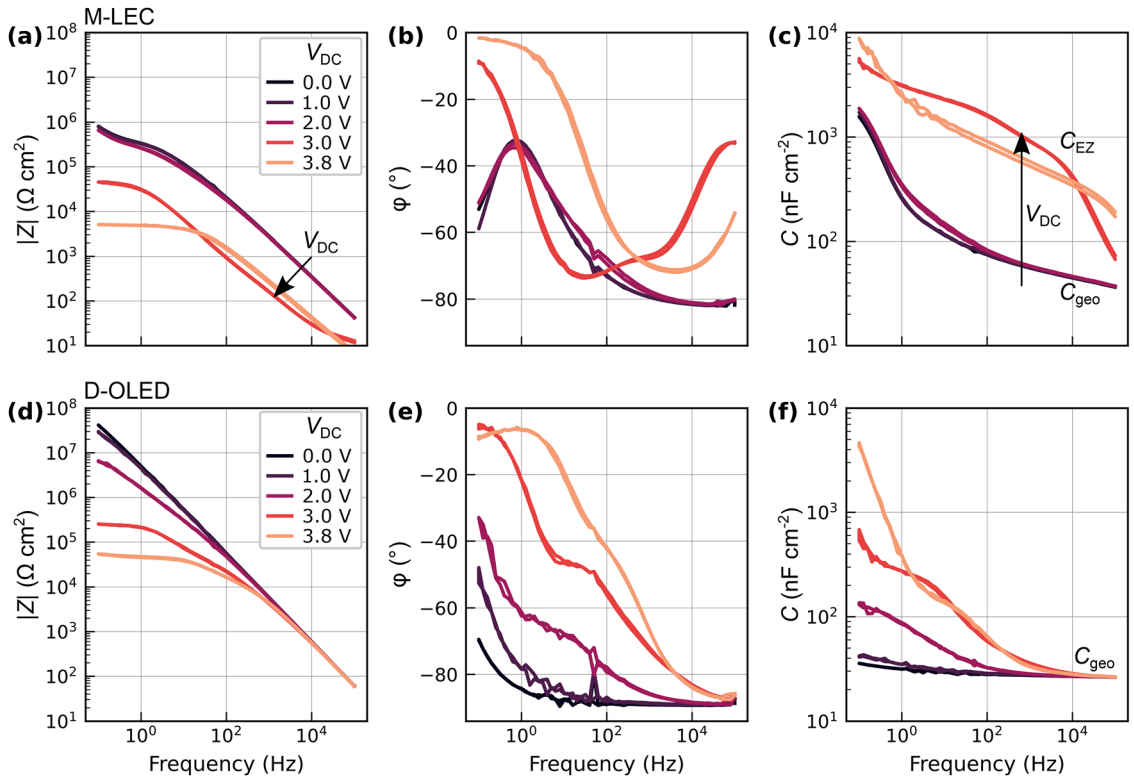

Fig. 4 IS data of (a–c) the M-LEC and (d–f) the D-OLED dependent on V_{DC}. We use VAC RMS = 20 mV and probe at T = 25 °C.

unaltered (EDLs form, but the AM remains undoped). For $V > E_{SY}/e$, which corresponds to a voltage where the LEC emits light, *cf.* Fig. 2, it transitions into a structure resembling a parallel $(RC)_{EZ}$ element, with R and C being the emission zone (EZ) resistance and capacitance. The EDLs become conductive, and C_{EDL} is now bypassed by a small charge-transfer resistance.[34] The EC-doped layers evolve, the thickness of the intrinsic OSC region shrinks, and the emission zone (EZ) forms between the p- and n-doped regions. As a result, the capacitance density of the LEC at high and intermediate frequencies changes from C_{geo} to C_{EZ}, the capacitance of the undoped EZ, *cf.* Fig. 4(c).[21,35] This transition of C_{geo} into C_{EZ} illustrates the LEC's doping process. The low-frequency impedance is dominated by the resistance of the undoped EZ, which now limits the DC in the device.

The D-OLED characteristics, *cf.* Fig. 4(d–f), also resemble a transition into the characteristics of a parallel (RC) element with increasing V_{DC}. But there are three notable differences compared to the LEC: First, the low-frequency values for $|Z|$ and φ start to decrease already for $V_{DC} < E_{SY}/e$. This implies that the injection-facilitating dipole reorientation of TMPE-OH is E-field driven rather than chemically induced following device fabrication. Second, for $V_{DC} > E_{SY}/e$, the sample does not show any change in C_{geo}. This proves that no doping and thus no p–i–n structure formation occurs. The AM remains undoped since it contains no ions. Third, for V_{DC} = 3.8 V, the low-frequency (or DC) resistance is about 10 times higher than for the M-LEC. This can be rationalized by the thickness difference of the undoped (DC limiting) region in both devices: While the LEC DC is limited by the EZ resistance (the EZ width is on the order of 0.1 d_{AM}),[40,42] the DC in the D-OLED is limited by the entire d_{AM}.

To explain the significantly lower driving voltage of the D-OLED compared to the N-OLED observed in Fig. 2, we can conclude from the IS experiments that it must be the injection resistance that is significantly reduced. IS showed that the D-OLED's AM exhibits a dipolar relaxation and that the device's DC impedance drops with increasing E-field while its high-frequency impedance remains unchanged, indicating that the dipole orientation facilitates bipolar charge injection into the semiconductor.

OLED characterization

Now that we have established how dipolar doping achieves bipolar injection, we test the generality of this strategy. For that purpose, we use four different polar molecular species blended into SY to fabricate D-OLEDs using the same device stack as before. Fig. S3 displays their voltage transients under constant-current operation for increasing doping concentration. We observe the same qualitative trend for all four dopants: with increasing dipole concentration, the driving voltage decreases, indicating dipole-mitigated injection for all four cases. When the doping level exceeds 50–60 wt%, however, the devices become prone to short-circuits, exhibit increased resistance, and are mostly non-functional. Such high dipolar doping levels yield poor film homogeneity and phase-separated domains, which potentially alter the SY packing and impair intermolecular charge-carrier transport.

All investigated dipolar dopants yield functional D-OLEDs with drastically enhanced forward luminance and reduced driving voltage, *cf.* Fig. S4(b–d), relative to the N-OLED shown in Fig. S4(a). Their optoelectronic performance depends on the properties of the dopants. While we initially chose TMPE-OH (M_n = 1014 g mol^{-1}) whose HOMO/LUMO levels are outside the SY levels, *cf.* Fig. 1(b), the lower-molecular-weight TMPE-OH (M_n = 450 g mol^{-1}), for which we measure HOMO/LUMO energies of −5.3 eV and −2.9 eV, respectively, appears to introduce traps in SY that improve charge-carrier balance but also reduce mobility. This leads to higher forward luminance and slightly increased driving voltage. Please refer to Fig. S4(b and c) for this comparison. As a further test, we replace SY with the sky-blue thermally activated delayed fluorescence (TADF) emitter 4TCzBN and dope it with TMPE-OH ($M_n \approx$ 450 g mol^{-1}), using the same device architecture as before. Again, we find decreasing driving voltages with increasing doping concentrations, *cf.* SI Section S6.

Finally, we compare the performance of the herein investigated D-OLED concept with SY-LECs and SY-OLEDs using dedicated injection layers. Fig. 5 shows the performance of the N-OLED (d_{AM} = 116 ± 5 nm) and the D-OLED (d_{AM} = 132 ± 5 nm) comprising TMPE-OH (M_n = 450 g mol^{-1}, 40 wt%) as the dopant. The current density–voltage–luminance (*JVL*) scans are conducted from 0 V to 7 V and back to 2 V in voltage steps of 0.1 V, each step taking 1 s, after pre-biasing the OLEDs for 10 s at 3 V. The N-OLED suffers from substantial injection resistance and shows no perceivable luminance beyond the sensitivity threshold of our setup, which is in agreement with the observations presented in Fig. 2. It also shows no significant *J–V* hysteresis, consistent with the IS data in Fig. 3(a–c), where we found no relaxation processes for the N-OLED. By blending TMPE-OH into the system, *cf.* Fig. 5(b), we achieve a D-OLED with greatly enhanced current and luminance performance, yielding low-voltage operation and a current efficacy above 10 cd A^{-1} at 100 cd m^{-2} during the return scan, *cf.* Fig. 5(c). The *E*-field dependence of the dipole orientation (the relaxation process found in Fig. 3) introduces hysteresis in both current and luminance.

This means that dipolar doping is a volatile, dynamic effect. It is therefore important to stress that the *JVL* characteristics of the D-OLED inherently depend on the measurement protocol and device history. Under constant-current operation, as typically used for lighting, this does not pose a significant limitation. For switchable applications such as displays, however, it may require that the pixel off-state be biased at a voltage close to the open-circuit voltage to maintain the dipole orientation. Nevertheless, the characteristics presented in Fig. 5 allow a meaningful comparison with previously reported SY devices: Niu, Blom, and coworkers reported a SY OLED comprising PEDOT:PSS and Ba as injection layers and a 120 nm thick SY film, achieving a current density of about 5 mA cm^{-2} at 5 V.[30] Burns, Yambem *et al.* presented a similar stack reaching about 1000 cd m^{-2} at 10 mA cm^{-2}, and a current efficacy of 10 cd A^{-1}.[43] For SY LECs, Diethelm, Hany, and coworkers reported similar current efficacies.[28] In our measurement, we reach approximately 5 and 7 mA cm^{-2} at 5 V and about 800 cd cm^{-2} at 10 mA cm^{-2}. Thus, our *JVL* values are comparable to those of SY-OLEDs featuring injection layers and SY-LECs.

Discussion

Concerning the dipolar compound, it may seem counterintuitive that large PEG-based polymers can reorient within a SY matrix, *cf.* SI Section S5. Instead of the entire polymer chain, however, only small segments like the ether (–C–O–C–) and hydroxyl (–O–H) groups may respond to the field. This reorientation still requires sufficiently large voids within the surrounding material and suggests that a soft, open, rubbery AM morphology is preferable to a dense, glassy, or crystalline one. Consequently, both the choice of the OSC and the AM's

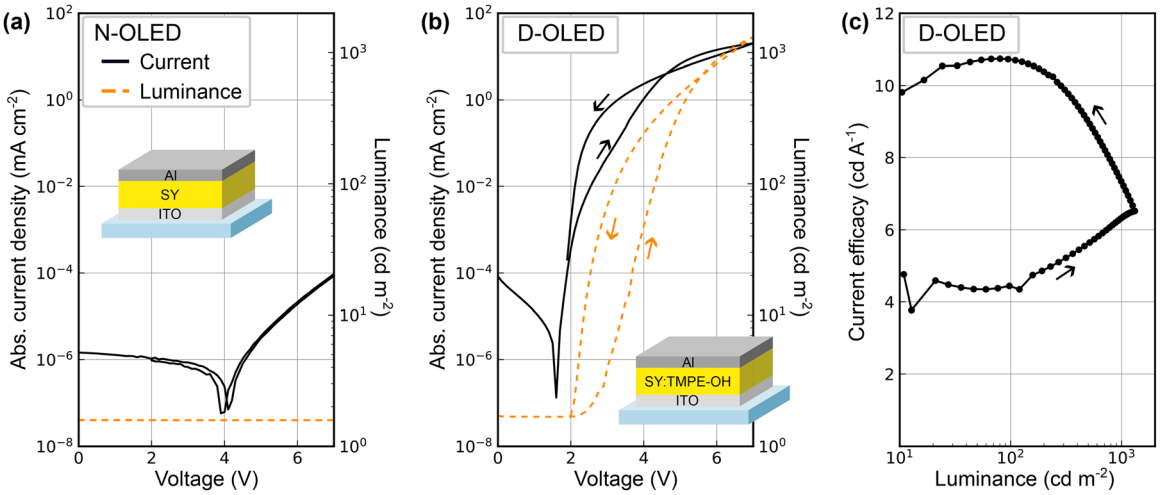

Fig. 5 JVL characterization of (a) the N-OLED and (b) D-OLED comprising a blend of SY:TMPE-OH (M_n = 450 g mol^{-1}, 40 wt%) as AM. (c) Current efficacy of the D-OLED.

deposition and annealing conditions likely play an important role in enabling *E*-field-induced dipole injection.

We further observe a notable increase in driving voltage for the D-OLED over time, *cf.* Fig. 2(a) and Fig. S4(b–d). As studied for PEO-based systems,[44,45] the terminal OH groups in TMPE-OH or the ether backbone are susceptible to oxidation at relatively low potentials.[46,47] TMPE-OH may thus act as a Brønsted acid, and deprotonation of the OH groups can produce hydrogen ions, leading to device degradation. We therefore suggest exploring other aprotic polar molecules.

Finally, the magnitude of the external *E*-field is an additional critical factor, since it exerts the torque that causes dipolar reorientation. In our devices, the initial magnitude of the *E*-field is on the order of 10–100 MV m^{-1}. This field will be partially screened when the dipoles in the AM orient and thereby form uncompensated charged layers at the two electrode interfaces, similar to EDLs in electrochemical devices or films that exhibit spontaneous orientation polarization.[26,48] However, a fundamental distinction of the herein reported strategy is that it does not depend on a long-range motion of bulky ions, avoids high voltages during fabrication,[23,24] and is instead activated and controlled by the *E*-field generated by the applied operating voltage.

Conclusion

We report a method for achieving bipolar charge injection from air-stable electrodes into a single organic film. This is achieved by blending an auxiliary dipolar compound into the OSC, a process referred to as dipolar doping. Under operation bias, these dipoles reorient in response to the applied *E*-field and yield injection-assisting EDLs at the electrode interfaces. Dipolar doping is advantageous for solution-based fabrication under ambient conditions because it is compatible with air-stable electrode materials, does not rely on the dipole orientation of the OSC or on mobile ions that can compromise device performance, avoids high voltages during fabrication, and eliminates the need for additional injection layers. We demonstrate the merits of this concept by fabricating a single-layer dipole OLED comprising the electroluminescent polymer SY and the dipolar compound TMPE-OH, which operates comparably to established multi-layer SY-OLEDs and LECs. We further show that efficient dipolar doping can be achieved with multiple dipolar molecules and a different emitter material. Thus, our approach is both practical and broadly applicable.

Experimental

Ink fabrication

The AM constituents are a phenyl-substituted poly(*para*-phenylenevinylene) copolymer termed ''Super Yellow'' (SY, Livilux PDY-132, Merck, Germany), a hydroxyl end-capped trimethylolpropane ethoxylate (TMPE–OH, M_n = 1014 g mol^{-1}, Merck, Germany), and a KCF_3SO_3 salt (Solvionic, France). The salt is dried in a vacuum oven at $p < 1$ mbar and 190 °C for 12 h and filtered with a 0.1 μm PTFE filter (Cytiva, Puradisc 25, Whatman) before use. TMPE-OH is dried in a vacuum oven at $p < 1$ mbar and 50 °C for 12 h. For the AM ink formulation, the constituents are separately dissolved in cyclohexanone (Sigma-Aldrich, USA) at a concentration of 10 mg mL^{-1} (SY), 20 mg mL^{-1} (TMPE–OH), and 10 mg ml^{-1} (KCF_3SO_3). They are stirred at 70 °C on a magnetic hot plate positioned in a glovebox ($[O_2] < 1$ ppm, $[H_2O] < 1$ ppm) for ≥ 24 h. For the formulation of the five AM inks, these master inks are blended in five different solute mass ratios (*cf.* Table 1). To yield a SY concentration of 7.25 mg ml^{-1} in the final ink, which determines the resulting AM film thickness, cyclohexanone is added accordingly. The final AM inks are then stirred again under the same conditions for ≥24 h. For the D-OLED presented in Fig. 5, a different TMPE–OH (M_n = 450 g mol^{-1}, Sigma-Aldrich, USA) is used.

Device fabrication

The indium tin oxide (ITO) coated (thickness = 145 nm, R_s = 20 Ω sq^{-1}) glass substrates (substrate area = 30 × 30 mm^2, thickness = 0.7 mm, Kintec, HK) are cleaned in an ultrasonic bath by sequentially using a detergent (Extran MA 01, Merck, GER) in deionized water, deionized water, acetone (VWR, GER), and isopropanol (VWR, GER). The ITO-coated substrates are dried in an oven at 120 °C for ≥ 12 h. The AM ink is spin-coated on the substrate (2000 rpm, acceleration = 2000 rpm s^{-1}, time = 60 s) and dried on a hot plate at 70 °C for 1 h. The AM thickness (d_{AM}) is measured with a stylus profilometer (Dektak XT, Bruker, USA). The values for d_{AM} are summarized in Table 1. The reflective Al top electrode (thickness = 100 nm) is deposited by thermal evaporation at a base pressure $p < 6 \times 10^{-6}$ mbar, with a shadow mask defining the cathode area. The spatial overlap between the cathode and the anode defines four 2 × 2 mm^2 LEC pixels on each substrate. For the IS and OLED *JVL* measurements, the devices are encapsulated with a cover glass (24 × 24 mm^2, VWR, GER) using a UV-curable epoxy resin (Ossila, UK) and measured under ambient conditions.

Device characterization

The voltage-luminance transients are recorded inside an N_2-filled glovebox ($[O_2]$, $[H_2O]$ < 1 ppm, T ≈ 22 °C). The devices are driven by a constant current of 0.31 mA, corresponding to a current density of J = 7.7 mA cm^{-2}, with the voltage compliance set to 21 V. The luminance is measured with a calibrated photodiode (S9219-01, Hamamatsu Photonics), and the voltage is tracked using a source measure unit (U2722A, Agilent).

The IS are recorded with the devices placed on a custom-built temperature stage to ensure a stabilized temperature of T = 25 ± 0.02 °C. The temperature stage comprises a Peltier element, powered by a DC power supply (E3631A Agilent) and monitored by a PT100 temperature sensor read by a multimeter (34401A Agilent). The feedback between the Peltier power supply and the temperature sensor is controlled using a Python-based PID controller.

The IS data are recorded by a potentiostat equipped with a frequency analyzer (Metrohm Autolab PGSTAT302). Before starting a frequency scan (100 kHz → 10 mHz → 100 kHz, 10 steps

per decade, V_{AC} RMS = 20 mV), the devices are stabilized at T = 25 ± 0.02 °C for 120 s to ensure thermal equilibrium. If $V_{DC} > 0$ is used, the devices remain biased for 1200 s before starting the measurement to ensure steady-state conditions. A few data points (mostly around the net frequency f = 50 Hz) exhibit unreasonable phase jumps and have been removed for clarity. Both the frequency analyzer and the temperature stage are controlled by SweepMe! (https://www.sweep-me.net), a multitool measurement software ensuring fully automated measurements.

For the OLED *JVL* characteristics, current and voltage are measured using a source measure unit (SMU, Keithley 2400) in a two-wire configuration. For the luminance data, a second SMU (Keithley 2400) measures the photocurrent generated by a photodiode (BPW21, Osram), equipped with an eye-response filter and calibrated using a luminance meter (Konica Minolta LS-110). All instruments are controlled by SweepMe!

Equivalent circuit model

The ECM displayed in Fig. 3(d) is modeled in Python using LTspice (Linear Technology), which contains a self-consistent, numerical frequency-domain solver for AC analysis. The AC amplitude is set to RMS = 20 mV, *i.e.* the same as in the measurement. The fixed parameter values for C_{geo} and C_{EDL} are directly taken from the experiment (Table 2). The free parameter R_{bulk} is chosen to match the experimental data. The full parameter set is given in the SI Section S4, and the Python script is available for download.

Author contributions

Anton Kirch: designed and conceptualized the study, acquired and analysed experimental data, mainly wrote the manuscript, and acquired funding. Joan Ràfols-Ribé: conceptualization, software, and setup development. Yuntao Qiu: fabrication and evaluation of TADF devices. Thushar Salkod Mahabaleshwar, William Strömberg: cyclic voltammetry measurements and evaluation. Ajay Kumar Poonia, Kumar Saumya: sample preparation and evaluation of SY-based devices. Preetam Dacha, Sri Harish Kumar Paleti: conceptualization and data analysis. Christian Larsen, Nicolò Maccaferri, Ludvig Edman: supervised the project, reviewed the data analysis and manuscript drafting, and acquired funding. All authors were involved in drafting and reviewing the manuscript and approved the final version to be published.

Conflicts of interest

The authors have no conflicts of interest to declare.

Data availability

All relevant data, SweepMe! setting files, and the Python script running the ECM AC analysis are available for download here: https://figshare.com/s/761a8ce7dcaee117bc8c.

Supplementary information (SI) is available. See DOI: https://doi.org/10.1039/d6mh00161k.

Acknowledgements

The authors acknowledge generous financial support from the Swedish Research Council (2019-02345 and 2021-04778), Kempe Foundations, Bertil och Britt Svenssons stiftelse för belysningsteknik, the Knut and Alice Wallenberg Foundation for a Proof-of-concept grant (KAW 2024.0497), and the Wallenberg Initiative Materials Science for Sustainability (WISE) funded by the Knut and Alice Wallenberg Foundation (WISE-AP01-D02 and WISE-AP02-PD21). L. E. acknowledges financial support from the European Union through an ERC Advanced Grant (ERC, InnovaLEC, 101096650). A. K. acknowledges funding from the European Union (HORIZON MSCA 2023 PF, acronym UNID, grant number 101150699). A. K. thanks Louis Conrad Winkler and Dr Jakob Wolansky (both TU Dresden, Germany) for their support with upgrading the Autolab SweepMe! driver. J. R. R. and A. K. thank Mikael Fredriksson and Peter Wikström for their support with crafting the temperature stage in the workshop. N. M. and A. K. P. acknowledge financial support from the Swedish Research Council (Grant No. 2021-05784), the Knut and Alice Wallenberg Foundation through the Wallenberg Academy Fellows Programme (Grant No. 2023.0089), and Kempestiftelserna (WISE-UmU/Kempe-program, Grant No. JCSMK 23-198).

References

1 J. H. Burroughes, D. D. C. Bradley, A. R. Brown, R. N. Marks, K. Mackay, R. H. Friend, P. L. Burns and A. B. Holmes, Light-Emitting Diodes Based on Conjugated Polymers, *Nature*, 1990, **347**(6293), 539–541, DOI: 10.1038/347539a0.

2 R. Su, S. H. Park, X. Ouyang, S. I. Ahn and M. C. McAlpine, 3D-Printed Flexible Organic Light-Emitting Diode Displays, *Sci. Adv.*, 2022, **8**(1), eabl8798, DOI: 10.1126/sciadv.abl8798.

3 A. J. Gillett, A. Privitera, R. Dilmurat, A. Karki, D. Qian, A. Pershin, G. Londi, W. K. Myers, J. Lee, J. Yuan, S.-J. Ko, M. K. Riede, F. Gao, G. C. Bazan, A. Rao, T.-Q. Nguyen, D. Beljonne and R. H. Friend, The Role of Charge Recombination to Triplet Excitons in Organic Solar Cells, *Nature*, 2021, **597**(7878), 666–671, DOI: 10.1038/s41586-021-03840-5.

4 Q. Burlingame, X. Huang, X. Liu, C. Jeong, C. Coburn and S. R. Forrest, Intrinsically Stable Organic Solar Cells under High-Intensity Illumination, *Nature*, 2019, **573**(7774), 394–397, DOI: 10.1038/s41586-019-1544-1.

5 M. Massetti, S. Zhang, P. C. Harikesh, B. Burtscher, C. Diacci, D. T. Simon, X. Liu, M. Fahlman, D. Tu, M. Berggren and S. Fabiano, Fully 3D-Printed Organic Electrochemical Transistors, *Npj Flex. Electron.*, 2023, **7**(1), 1–11, DOI: 10.1038/s41528-023-00245-4.

6 J. Schröder, A. Bonil, L. C. Winkler, J. Frede, G. Darbandy, J. Wang, K. Leo, H. Kleemann and J. Benduhn, Organic Permeable Base Transistors for High-Performance

Photodetection with Photo-Memory Effect, *Nat. Photonics*, 2025, **19**(10), 1088–1098, DOI: 10.1038/s41566-025-01740-y.

7 J. Wolansky, C. Hoffmann, M. Panhans, L. C. Winkler, F. Talnack, S. Hutsch, H. Zhang, A. Kirch, K. M. Yallum, H. Friedrich, J. Kublitski, F. Gao, D. Spoltore, S. C. B. Mannsfeld, F. Ortmann, N. Banerji, K. Leo and J. Benduhn, Sensitive Self-Driven Single-Component Organic Photodetector Based on Vapor-Deposited Small Molecules, *Adv. Mater.*, 2024, **36**(50), 2402834, DOI: 10.1002/adma.202402834.

8 A. Kirch, T. Bärschneider, T. Achenbach, F. Fries, M. Gmelch, R. Werberger, C. Guhrenz, A. Tomkevičienė, J. Benduhn, A. Eychmüller, K. Leo and S. Reineke, Accurate Wavelength Tracking by Exciton Spin Mixing, *Adv. Mater.*, 2022, **34**(38), 2205015, DOI: 10.1002/adma.202205015.

9 R. Kantelberg, T. Achenbach, A. Kirch and S. Reineke, In-Plane Oxygen Diffusion Measurements in Polymer Films Using Time-Resolved Imaging of Programmable Luminescent Tags, *Sci. Rep.*, 2024, **14**(1), 5826, DOI: 10.1038/s41598-024-56237-5.

10 S. R. Forrest, The Path to Ubiquitous and Low-Cost Organic Electronic Appliances on Plastic, *Nature*, 2004, **428**(6986), 911, DOI: 10.1038/nature02498.

11 R. R. Nair, J. Wolansky, K. Uhlig, A. Solgi, L. Teuerle, T. Zhang, J. Schröder, T. Antrack, J. Benduhn, H. Kleemann and K. Leo, Leaftronics: Natural Lignocellulose Scaffolds for Sustainable Electronics, *Sci. Adv.*, 2024, **10**(45), eadq3276, DOI: 10.1126/sciadv.adq3276.

12 C. Larsen, P. Lundberg, S. Tang, J. Ràfols-Ribé, A. Sandström, E. Mattias Lindh, J. Wang and L. Edman, A Tool for Identifying Green Solvents for Printed Electronics, *Nat. Commun.*, 2021, **12**(1), 4510, DOI: 10.1038/s41467-021-24761-x.

13 A. Sandström, A. Asadpoordarvish, J. Enevold and L. Edman, Spraying Light: Ambient-Air Fabrication of Large-Area Emissive Devices on Complex-Shaped Surfaces, *Adv. Mater.*, 2014, **26**(29), 4975–4980, DOI: 10.1002/adma.201401286.

14 S. Reineke, F. Lindner, G. Schwartz, N. Seidler, K. Walzer, B. Lüssem and K. Leo, White Organic Light-Emitting Diodes with Fluorescent Tube Efficiency, *Nature*, 2009, **459**(7244), 234–238, DOI: 10.1038/nature08003.

15 A. Kirch, A. Fischer, R. Werberger, S. M. Aabi Soflaa, K. Maleckaite, P. Imbrasas, J. Benduhn and S. Reineke, Simple Strategy to Measure the Contact Resistance between Metals and Doped Organic Films, *Phys. Rev. Appl.*, 2022, **18**(3), 034017, DOI: 10.1103/PhysRevApplied.18.034017.

16 I. H. Campbell, S. Rubin, T. A. Zawodzinski, J. D. Kress, R. L. Martin, D. L. Smith, N. N. Barashkov and J. P. Ferraris, Controlling Schottky Energy Barriers in Organic Electronic Devices Using Self-Assembled Monolayers, *Phys. Rev. B: Condens. Matter Mater. Phys.*, 1996, **54**(20), R14321–R14324, DOI: 10.1103/PhysRevB.54.R14321.

17 T.-F. Guo, F.-S. Yang, Z.-J. Tsai, T.-C. Wen, S.-N. Hsieh and Y.-S. Fu, High-Performance Polymer Light-Emitting Diodes Utilizing Modified Al Cathode, *Appl. Phys. Lett.*, 2005, **87**(1), 013504, DOI: 10.1063/1.1984101.

18 Q. Pei, G. Yu, C. Zhang, Y. Yang and A. J. Heeger, Polymer Light-Emitting Electrochemical Cells, *Science*, 1995, **269**(5227), 1086–1088, DOI: 10.1126/science.269.5227.1086.

19 Y. Noguchi, H. Lim, T. Isoshima, E. Ito, M. Hara, W. Won Chin, J. Wook Han, H. Kinjo, Y. Ozawa, Y. Nakayama and H. Ishii, Influence of the Direction of Spontaneous Orientation Polarization on the Charge Injection Properties of Organic Light-Emitting Diodes, *Appl. Phys. Lett.*, 2013, **102**(20), 203306, DOI: 10.1063/1.4807797.

20 A. J. L. Hofmann, S. Züfle, K. Shimizu, M. Schmid, V. Wessels, L. Jäger, S. Altazin, K. Ikegami, M. R. Khan, D. Neher, H. Ishii, B. Ruhstaller and W. Brütting, Dipolar Doping of Organic Semiconductors to Enhance Carrier Injection, *Phys. Rev. Appl.*, 2019, **12**(6), 064052, DOI: 10.1103/PhysRevApplied.12.064052.

21 J. Ràfols-Ribé, A. Sato, A. Kirch, X. Zhang, S. Jenatsch, C. Larsen, K. Marumoto and L. Edman, Pinpointing the Dynamic P-i-n Junction, *PRX Energy*, 2025, **4**(3), 033015, DOI: 10.1103/2vyr-4yp3.

22 J. Fang, P. Matyba, N. D. Robinson and L. Edman, Identifying and Alleviating Electrochemical Side-Reactions in Light-Emitting Electrochemical Cells, *J. Am. Chem. Soc.*, 2008, **130**, 4562–4568, DOI: 10.1021/ja7113294.

23 F. Cui, J. Qiao, Y. Xu, Z. Fu, R. Gui, C. Zhang, R. Zhou, L. Ye, X. Du, F. Chen, X. Hao, H. Yan and H. Yin, Using an External Electric Field to Tune Active Layer Morphology Enabling High-Efficiency Organic Solar Cells via Ambient Blade Coating, *Sci. Adv.*, 2024, **10**(26), eado5460, DOI: 10.1126/sciadv.ado5460.

24 Y. Zhao, M. Gao, Y. Qin, X. Da, X. Deng, X. Jia, K. Xi, Y. Su, S. Ding, Q. Rong, X. Kong and G. Gao, Electric Field Induced Molecular Orientation to Construct the Composite Polymer Electrolytes with Vertically Aligned Ion Diffusion Pathways for Stable Solid-State Lithium Metal Batteries, *Chem. Eng. J.*, 2024, **495**, 153645, DOI: 10.1016/j.cej.2024.153645.

25 M. Rodríguez-López, M. Gonzalez-Silveira, A. Cappai, R. Dettori, C. Rodríguez-Tinoco, C. Melis, L. Colombo and J. Rodríguez-Viejo, Manipulating Molecular Orientation in Vapor-Deposited Organic Semiconductor Glasses via in Situ Electric Fields: A Molecular Dynamics Study, *J. Mater. Chem. C*, 2024, **12**(44), 18111–18120, DOI: 10.1039/D4TC03271C.

26 A. Hofmann, M. Schmid and W. Brütting, The Many Facets of Molecular Orientation in Organic Optoelectronics, *Adv. Opt. Mater.*, 2021, **9**(21), 2101004, DOI: 10.1002/adom.202101004.

27 X. Jin, A. Sandström, E. M. Lindh, W. Yang, S. Tang and L. Edman, Challenging Conventional Wisdom: Finding High-Performance Electrodes for Light-Emitting Electrochemical Cells, *ACS Appl. Mater. Interfaces*, 2018, **10**(39), 33380–33389, DOI: 10.1021/acsami.8b13036.

28 M. Diethelm, Q. Grossmann, A. Schiller, E. Knapp, S. Jenatsch, M. Kawecki, F. Nüesch and R. Hany, Optimized Electrolyte Loading and Active Film Thickness for Sandwich Polymer Light-Emitting Electrochemical Cells, *Adv. Opt. Mater.*, 2019, **7**(3), 1801278, DOI: 10.1002/adom.201801278.

29 A. Kirch, S.-R. Park, J. Ràfols-Ribé, J. A. Kassel, X. Zhang, S. Tang, C. Larsen and L. Edman, Impact of the Electrode Material on the Performance of Light-Emitting Electrochemical Cells, *ACS Appl. Mater. Interfaces*, 2025, **17**(3), 5184–5192, DOI: 10.1021/acsami.4c18009.

30 Q. Niu, G.-J. A. H. Wetzelaer, P. W. M. Blom and N. I. Crăciun, Modeling of Electrical Characteristics of Degraded Polymer Light-Emitting Diodes, *Adv. Electron. Mater.*, 2016, **2**(8), 1600103, DOI: 10.1002/aelm.201600103.

31 J. Fang, P. Matyba and L. Edman, The Design and Realization of Flexible, Long-Lived Light-Emitting Electrochemical Cells, *Adv. Funct. Mater.*, 2009, **19**(16), 2671–2676, DOI: 10.1002/adfm.200900479.

32 *Trimethylolpropane ethoxylate average Mn 1,014 50586-59-9*. https://www.sigmaaldrich.com/SE/en/product/aldrich/416177 (accessed 2025-07-02).

33 A. Kirch, J. Wolansky, S. Miri Aabi Soflaa, S. A. Buchholtz, R. Werberger, C. Kaiser, A. Fischer, K. Leo, L. Edman, J. Benduhn and S. Reineke, Tuning Charge-Transfer States by Interface Electric Fields, *ACS Appl. Mater. Interfaces*, 2024, **16**(24), 31407–31418, DOI: 10.1021/acsami.4c04602.

34 A. Ch Lazanas and M. I. Prodromidis, Electrochemical Impedance Spectroscopy-A Tutorial, *ACS Meas. Sci. Au*, 2023, **3**(3), 162–193, DOI: 10.1021/acsmeasuresciau.2c00070.

35 A. Munar, A. Sandström, S. Tang and L. Edman, Shedding Light on the Operation of Polymer Light-Emitting Electrochemical Cells Using Impedance Spectroscopy, *Adv. Funct. Mater.*, 2012, **22**(7), 1511–1517, DOI: 10.1002/adfm.201102687.

36 S. van Reenen, P. Matyba, A. Dzwilewski, R. A. J. Jenssen, L. Edman and M. Kemerink, Salt Concentration Effects in Planar Light-Emitting Electrochemical Cells, *Adv. Funct. Mater.*, 2011, **21**(10), 1795–1802, DOI: 10.1002/adfm.201002360.

37 C. Porter and R. Boyd, A Dielectric Study of the Effects of Melting on Molecular Relaxation in Poly(Ethylene Oxide) and Polyoxymethylene, *Macromolecules*, 1971, **4**(5), 589–594, DOI: 10.1021/ma60023a015.

38 K. P. Singh and P. N. Gupta, Study of Dielectric Relaxation in Polymer Electrolytes, *Eur. Polym. J.*, 1998, **34**(7), 1023–1029, DOI: 10.1016/S0014-3057(97)00207-3.

39 M. C. Schmidt, A. O. Alvarez, J. J. de Boer, L. J. M. van de Ven and B. Ehrler, Consistent Interpretation of Time- and Frequency-Domain Traces of Ion Migration in Perovskite Semiconductors, *ACS Energy Lett.*, 2024, **9**(12), 5850–5858, DOI: 10.1021/acsenergylett.4c02446.

40 S. van Reenen, R. A. J. Janssen and M. Kemerink, Dynamic Processes in Sandwich Polymer Light-Emitting Electrochemical Cells, *Adv. Funct. Mater.*, 2012, **22**(21), 4547–4556, DOI: 10.1002/adfm.201200880.

41 M. Frank and J. Pflaum, Tuning Electronic and Ionic Transport by Carbon-Based Additives in Polymer Electrolytes for Thermoelectric Applications, *Adv. Funct. Mater.*, 2022, **32**(32), 2203277, DOI: 10.1002/adfm.202203277.

42 X. Zhang, J. Ràfols-Ribé, A. Kirch, C. Larsen and L. Edman, Determining the Width of the Dynamic Emission Zone in Light-Emitting Electrochemical Cells, *Adv. Opt. Mater.*, 2025, **13**(22), 2501128, DOI: 10.1002/adom.202501128.

43 S. Burns, J. MacLeod, T. Trang Do, P. Sonar and S. D. Yambem, Effect of Thermal Annealing Super Yellow Emissive Layer on Efficiency of OLEDs, *Sci. Rep.*, 2017, **7**(1), 40805, DOI: 10.1038/srep40805.

44 J. Feng, L. Wang, Y. Chen, P. Wang, H. Zhang and X. He, PEO Based Polymer-Ceramic Hybrid Solid Electrolytes: A Review, *Nano Converg*, 2021, **8**, 2, DOI: 10.1186/s40580-020-00252-5.

45 X. Yang, M. Jiang, X. Gao, D. Bao, Q. Sun, N. Holmes, H. Duan, S. Mukherjee, K. Adair, C. Zhao, J. Liang, W. Li, J. Li, Y. Liu, H. Huang, L. Zhang, S. Lu, Q. Lu, R. Li, C. Veer Singh and X. Sun, Determining the Limiting Factor of the Electrochemical Stability Window for PEO-Based Solid Polymer Electrolytes: Main Chain or Terminal –OH Group?, *Energy Environ. Sci.*, 2020, **13**(5), 1318–1325, DOI: 10.1039/D0EE00342E.

46 S. Tang, J. Mindemark, C. M. G. Araujo, D. Brandell and L. Edman, Identifying Key Properties of Electrolytes for Light-Emitting Electrochemical Cells, *Chem. Mater.*, 2014, **26**(17), 5083–5088, DOI: 10.1021/cm5022905.

47 J. Mindemark, S. Tang, J. Wang, N. Kaihovirta, D. Brandell and L. Edman, High-Performance Light-Emitting Electrochemical Cells by Electrolyte Design, *Chem. Mater.*, 2016, **28**(8), 2618–2623, DOI: 10.1021/acs.chemmater.5b04847.

48 Y. Noguchi, W. Brütting and H. Ishii, Spontaneous Orientation Polarization in Organic Light-Emitting Diodes, *Jpn. J. Appl. Phys.*, 2019, **58**(SF), SF0801, DOI: 10.7567/1347-4065/ab0de8.